Electronic Supplementary Information (ESI)

A metal organic framework-derived octahedral $Cu_{1.95}S@CoS_2$ for secondary batteries displaying long cycle life and stable temperature tolerance

Tianli Han[a,*], Haiyuan Bai[a], Jing Xu[a], Yajun Zhu[a,b], Xirong Lin[c], Jinyun Liu[a,*]

Experimental details

Preparation of Cu-MOF: 1.1545 g $Cu(NO_3)_3 \cdot 3H_2O$ was dissolved in 15 mL of DMF to form asolution A, and 0.6145 g H_3BTC was dissolved in 15 mL of DMF to form a solution B. Then, 0.4389 g PVP was added to solution A and stirred for 10 min to form a mixed solution. After that, solution B was slowly added to solution A and stirred for 1 h. The mixture was poured into a teflon-liner and reacted in an autoclave at 80 °C for 24 h. The precipitate was washed by DMF and ethanol, and dried at 70 °C for 12 h.

Preparation of Cu-MOF@Co-MOF: In this experiment, 0.2 g Cu-MOF was dispersed in 50 mL of methanol by ultrasound for 10 min. Then, 0.821 g dimethylimidazole was dissolved into 50 mL of methanol and added into the above solution. At the same time, 0.582 g $Co(NO_3)_2 \cdot 6H_2O$ was added into the above solution and stirred for one h. After the stirring, the mixed solution was kept at room temperature for 6 h, then the precipitate was collected and washed by ethanol, and dried at 70 °C for 12 h.

Preparation of $Cu_{1.95}S@CoS_2$ composite: 3 g sulfur powder and 0.15 g Cu-MOF@Co-MOF were placed on both sides of the porcelain boat, and the porcelain boat was placed in a tubular furnace. Among them, the sulfur powder is located in the

upstream of the vent. In the atmosphere of Ar, the tubular furnace was heated to 500 °C at the rate of 2 °C/min and maintained for 1 h. At last, the sample was collected for further use.

Characterizations: The crystal structure and phase analysis were measured by XRD diffractometer (XRD SMART APEX II Brook, Cu Kα X-ray wavelength=1.5418 Å). Scanning electron microscope (SEM, Hitachi 8100, 5 KV) and transmission electron microscope (TEM, Hitachi HT-7700, 120 KV) were used to observe the microstructure of sample. The lattice fringes of the sample were observed by high resolution transmission electron microscopy (HRTEM, TecnaiG220S-Twin, 200 KV). Energy-dispersive X-ray spectroscopy (EDX, Hitachi 8100, 15 KV) was applied to analyzed element mapping and composition. The binding energy of the sample and valence distribution of the element were investigated by X-ray photoelectron spectroscopy (XPS, EscalAB250, Al Kα hν=1486.6 eV). Adsorption-desorption curves and Brunauer-Emmett-Teller (BET) specific surface area of the sample were measured by ASAP Micromeritics Tristar 2460 instrument.

Electrochemical tests: $Cu_{1.95}S@CoS_2$ (70 wt%) and conductive carbon black (20 wt%) were thoroughly mixed and ground for 30 min, then the polyvinylidene fluoride (PVDF, 6.54%, 10 wt%) was added as a binder. Subsequently, a few drops of N-methylpyrrolidone (NMP, 99.99%) was added as a dispersant to make it into a slurry. After stirring for 8 h, the paste is evenly coated on the carbon paper with a thickness of about 200 μm. The carbon paper loaded with stock was dried in a vacuum oven for 24 h and then cut into electrode pieces of 1.13 cm^2. The anode was pure aluminum sheet, the diaphragm was glass fiber, and the electrolyte composition was $AlCl_3$:[EMIm]Cl=1.3:1. Before assembling the battery, a molybdenum sheet with a thickness of 0.02 mm and a diameter of 20 mm is added to the cathode shell to prevent the corrosion of the battery shell by the electrolyte. The battery was assembled in a glove box (MIKROUNA, Super1220/750/900) filled with Ar, which both water and oxygen value were less than 0.01 ppm. In the voltage range of 0.01-1.9 V, the cyclic

and rate performance of the battery are measured by galvanostatic method. The *ex-situ* XRD was investigated by XRD diffractometer (XRD SMART APEX II Brook, Cu Kα X-ray wavelength=1.5418 Å). Cyclic voltammetry (CV) curves and Electrochemical impedance spectroscopy (EIS) were measured by electrochemical workstation (CHI660e). *In-situ* interface impedance was investigated by galvanostatic intermittent titration technique (GITT).

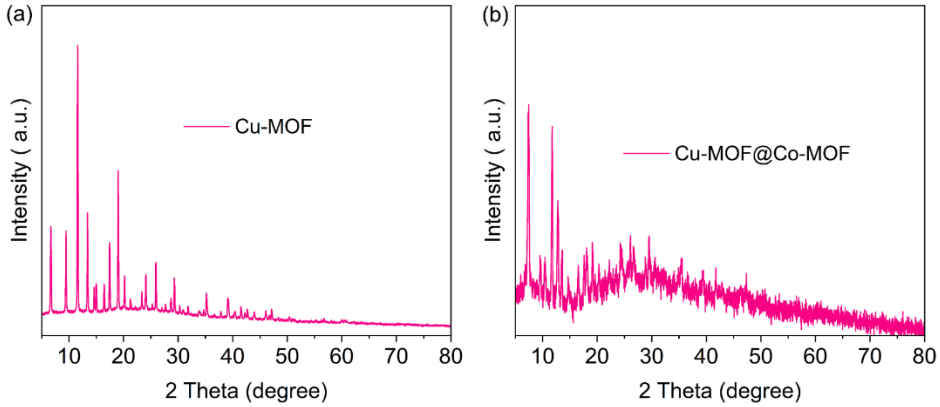

Fig. S1 XRD patterns of (a) Cu-MOF and (b) Cu-MOFs@Co-MOF.

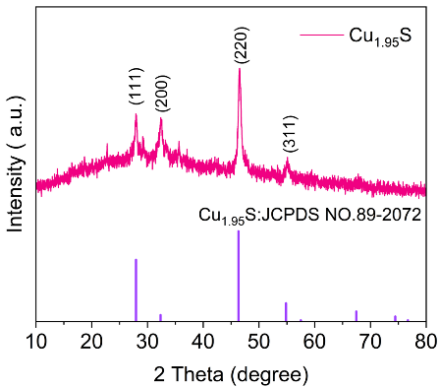

Fig. S2 XRD patterns of $Cu_{1.95}S$.

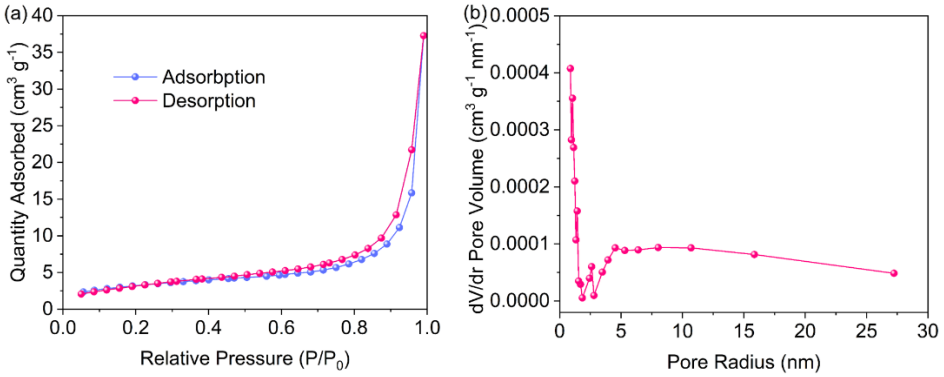

Fig. S3 (a) N_2 adsorption-desorption isotherms and (b) pore-size distribution of $Cu_{1.95}S$.

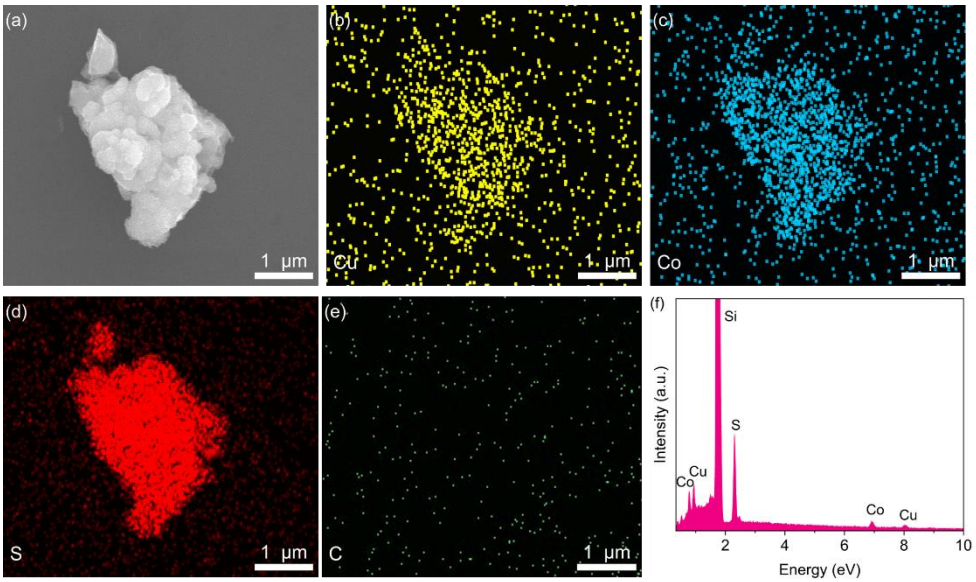

Fig. S4 (a) SEM image and (b-e) elemental mappings of $Cu_{1.95}S@CoS_2$. (f) EDS spectrum of $Cu_{1.95}S@CoS_2$.

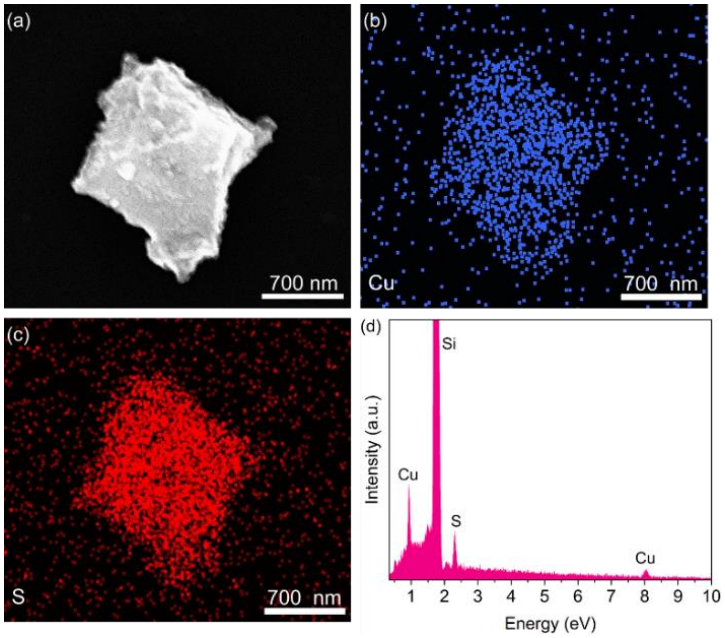

Fig. S5 (a) SEM image of $Cu_{1.95}S$. (b,c) The corresponding elemental mappings. (e) EDS spectrum of $Cu_{1.95}S$.

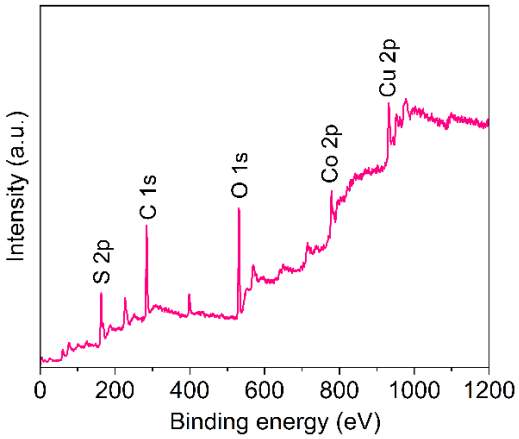

Fig. S6 XPS full spectrum of $Cu_{1.95}S@CoS_2$.

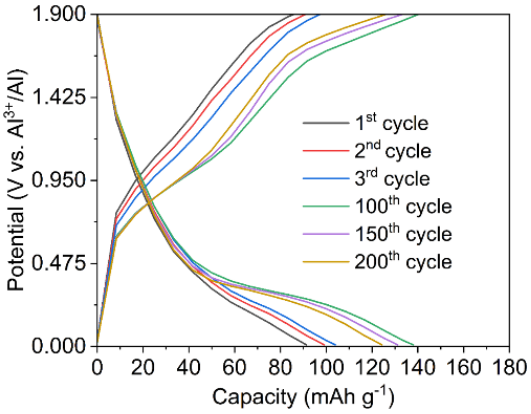

Fig. S7 Charge-discharge curves of $Cu_{1.95}S@CoS_2$ cathode at –10 °C.

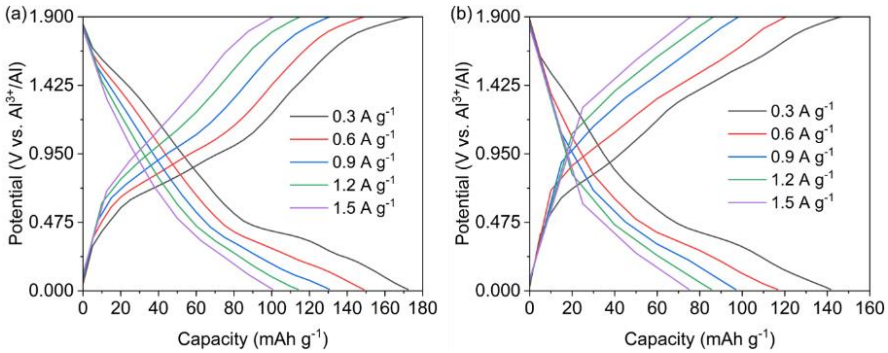

Fig. S8 Charge-discharge curves of (a) $Cu_{1.95}S@CoS_2$ and (b) $Cu_{1.95}S$ cathode at various current densities.

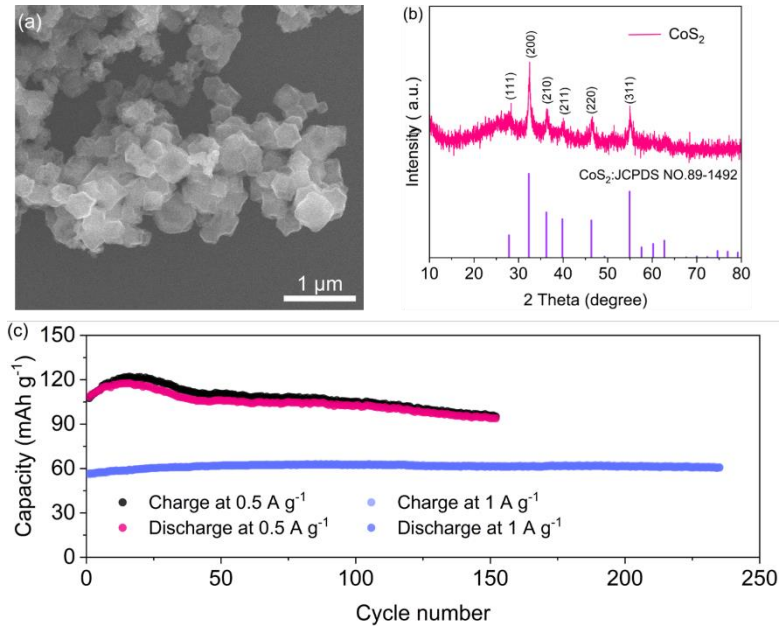

Fig. S9 (a) SEM image of CoS_2. (b) XRD patterns of CoS_2. (c) Cycling performance of CoS_2 cathode at 0.5 A g^{-1} and 1 A g^{-1}.

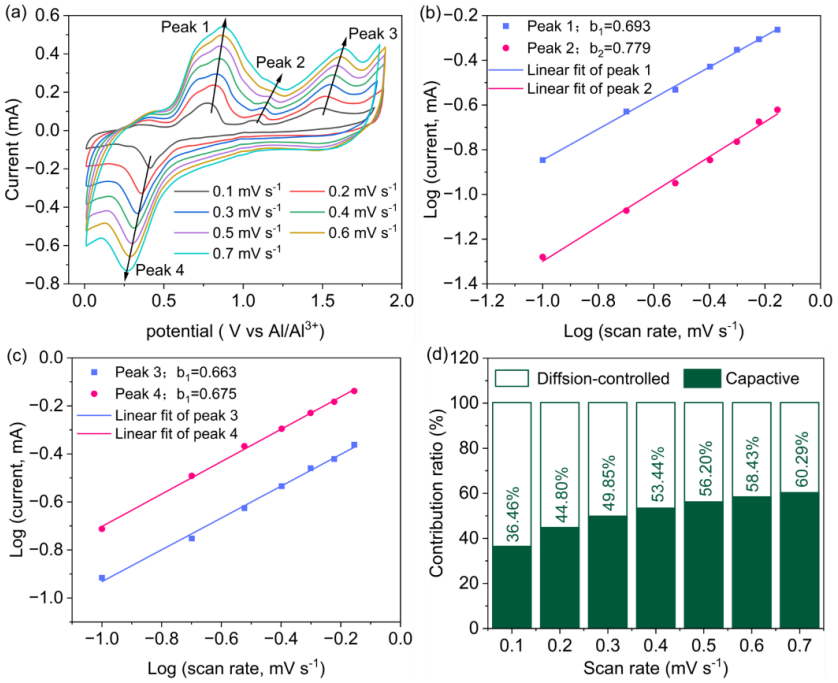

Fig. S10 (a) CV curves of $Cu_{1.95}S$ cathode from 0.1 to 0.7 mV s^{-1}. (b, c) Log(*v*) to log(*i*) linear analysis. (d) Ratios of capacitance and diffusion contribution.

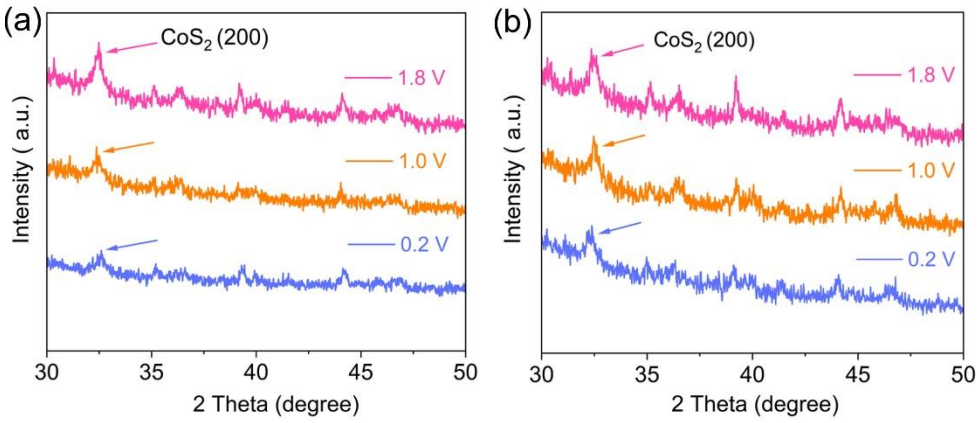

Fig. S11 *Ex situ* XRD patterns of $Cu_{1.95}S@CoS_2$ in (a) discharge and (b) charge.

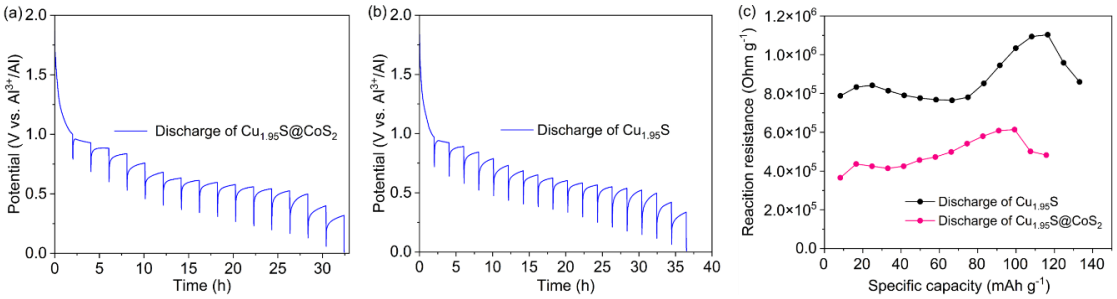

Fig. S12 GITT time-potential curves of (a) $Cu_{1.95}S@CoS_2$ and (b) $Cu_{1.95}S$ cathode during discharge. (c) *In-situ* interface reaction resistance of $Cu_{1.95}S@CoS_2$ and $Cu_{1.95}S$ cathode.

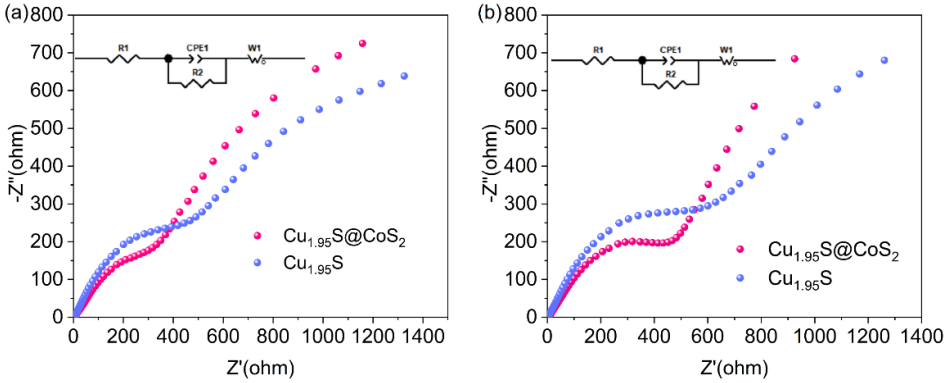

Fig. S13 EIS spectra of $Cu_{1.95}S@CoS_2$ and $Cu_{1.95}S$ (a) before and (b) after 100 cycles at 0.5 A g^{-1}.

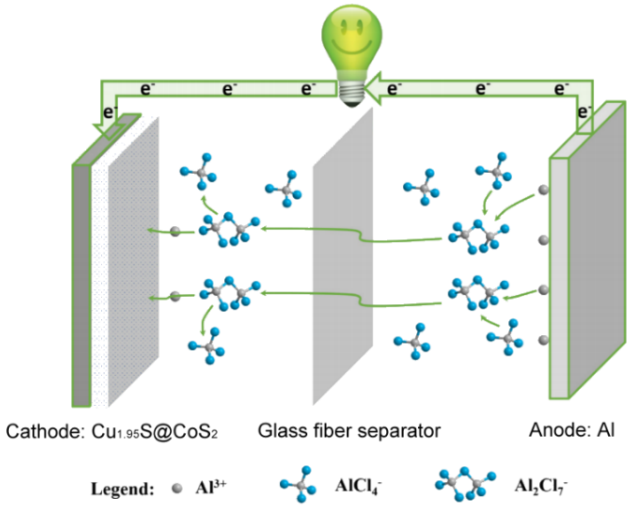

Fig. S14 Schematic diagram of reaction principle in the discharge process of Al-ion battery.

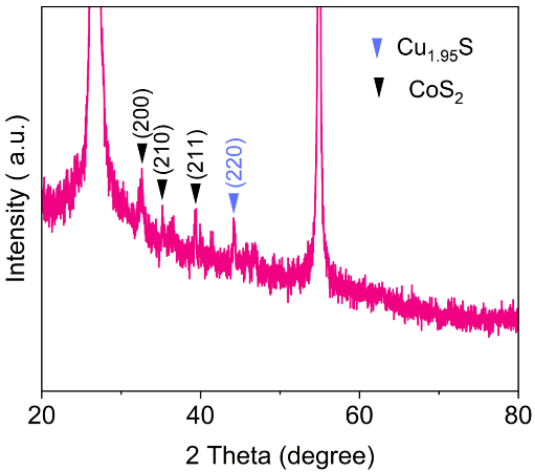

Fig. S15 XRD patterns of $Cu_{1.95}S@CoS_2$ after 100 cycles at 0.5 A g^{-1}.

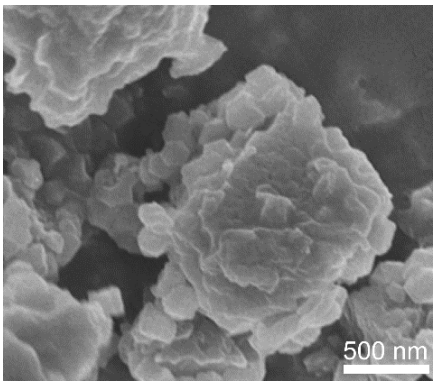

Fig. S16 SEM image of $Cu_{1.95}S@CoS_2$ after 100 cycles at 0.5 A g^{-1}.

Table S1. Comparison of Al-ion battery performance among many cathode materials.

Materials	Current density ($A\ g^{-1}$)	Cycle number	Capacity ($mAh\ g^{-1}$)	Ref.
$Cu_{2-x}Se$ nanorods	0.2	100	100	1
VO_2 nanorods	0.05	100	116	2
	0.1	100	106	
Co_3O_4 polyhedrons	0.1	100	31	3
Co_3O_4@MWCNTs polyhedrons	0.1	150	125	3
CoS_2@CNTs	0.1	100	60	4
MoS_2 microspheres	0.05	100	112.2	5
	0.1	150	58.5	
MoO_2@Ni	0.1	100	25	6
TiO_2 nanorods	0.5	150	91	7
CuS@C microspheres	0.02	100	90	8
$Cu_{1.81}Te$ nanorods	0.04	66	50	9
ZnSe@$SnSe_2$ microcubes	0.2	100	100	10
$Cu_{1.95}S$@CoS_2	0.5	200	136.6	This work
	1	500	96.9	

References

[1] J. Jiang, H. Li, T. Fu, B. Hwang, X. Li and J. Zhao, *ACS Appl. Mater. Interfaces*, 2018, **10**, 17942−17949.

[2] W. Wang, B. Jiang, W. Xiong, H. Sun, Z. Lin, L. Hu, J. Tu, J. Hou, H. Zhu and S. Jiao, *Sci. Rep.*, 2013, **3**, 3383.

[3] X. Xiao, M. Wang, J. Tu, Y. Luo and S. Jiao, *ACS Sustainable Chem. Eng.*, 2019, **7**, 16200−16208.

[4] K. Zhang, T. Lee, J. Cha, H. Jang, M. Shokouhimehr and J. Choi, *Electron. Mater. Lett.*, 2019, **15**, 727−732.

[5] J. Tu, X. Xiao, M. Wang and S. Jiao, *J. Phys. Chem. C*, 2019, **123**, 26794−26802.

[6] J. Wei, W. Chen, D. Chen and K. Yang, *J. Electrochem. Soc.*, 2017, **164**, A2304−A2309.

[7] S. Wang, K. V. Kravchyk, S. Pigeot-Remy, W. Tang, F. Krumeich, M. Wörle, M. I. Bodnarchuk, S. Cassaignon, O. Durupthy, S. Zhao, C. Sanchez and M. V. Kovalenko, *ACS Appl. Nano Mater.*, 2019, **2**, 6428−6435.

[8] S. Wang, S. Jiao, J. Wang, H. Chen, D. Tian, H. Lei and D. Fang, *ACS Nano*, 2017, **11**, 469−477.

[9] J. Wu, D. Wu, M. Zhao, Z. Wen, J. Jiang, J. Zeng and J. Zhao, *Dalton Trans.*, 2020, **49**, 729–736.

[10] J. Li, W. Luo, Z. Zhang, F. Li, Z. Chao, J. Fan, *J. Colloid Interf. Sci.*, 2023, **639**, 124–132.